coatings

MDPI

Article

A Laser-Engineered Architecture for a Thermally Switchable Slippery Surface with Durable Anti-Corrosion and Self-Healing Properties

Zexu Zhao, Guoyun Luo, Yuchao Li and Lijun Song *

State Key Laboratory of Advanced Design and Manufacturing Technology for Vehicle, Hunan Provincial Key Laboratory of Intelligent Laser Manufacturing, Hunan University, Changsha 410082, China; zhaozexu@hnu.edu.cn (Z.Z.)

* Correspondence: ljsong@hnu.edu.cn

Abstract

Slippery lubricant-infused surfaces (SLIPS) suffer from rapid lubricant depletion, severely limiting their durability in practical applications. To overcome this, we propose a laser-engineered hierarchical architecture that physically locks a solid paraffin lubricant, creating a multifunctional coating with thermally switchable slipperiness. Using femtosecond laser ablation, a hierarchical porous structure (HPS) was fabricated on an aluminum alloy, followed by silanization to achieve superhydrophobicity (contact angle ≈ 154.7°) for enhanced paraffin wetting. The resulting HPS-P coating exhibits thermally switchable adhesion: water droplets pin on the solid surface (sliding angle > 90°) but slide readily (<10°) upon heating above the paraffin's melting point. The coating demonstrates rapid self-healing, repairing severe scratches within 100 s via molten paraffin flow. The HPS-P coating provides excellent corrosion protection, with its corrosion current density reduced by six orders of magnitude compared to bare aluminum and an inhibition efficiency approaching 100%. This work provides a durable, thermally responsive coating strategy with integrated anti-corrosion and self-healing functions for extreme environments.

Keywords: SLIPS; femtosecond laser; hierarchical porous structure; corrosion; self-healing anti-corrosion coating; phase-change lubricant

1. Introduction

Slippery lubricant-infused porous surfaces (SLIPS), inspired by the Nepenthes pitcher plant, are widely recognized for their liquid-repelling behavior under low tilting angles [1]. By maintaining a stable, continuous, immiscible liquid layer over a micro/nanostructured substrate, SLIPS achieve exceptional repellency and are widely applied in anti-icing [2,3], anti-corrosion [4,5], self-healing [6] and anti-biofouling [7]. Despite these advantages, the transition of SLIPS to practical, long-term engineering applications is largely limited by lubricant depletion [8,9]. In practical applications, environmental factors like shear forces, evaporation, or mechanical damage cause the infused lubricant to escape from the porous network. This loss leads to rapid degradation of the surface protection functions, rendering traditional SLIPS unreliable in harsh environments such as marine infrastructure. In marine engineering, aluminum alloys are indispensable lightweight structural materials, yet their vulnerability to chloride-induced corrosion significantly reduces their service life and structural integrity [10]. Therefore, creating a durable, smart coating that can protect aluminum alloys in such harsh environments represents a critical technological challenge.

Check for updates

Academic Editor: Maria Vittoria Diamanti

Received: 26 February 2026
Revised: 7 March 2026
Accepted: 11 March 2026
Published: 13 March 2026

Copyright: © 2026 by the authors. Licensee MDPI, Basel, Switzerland. This article is an open access article distributed under the terms and conditions of the Creative Commons Attribution (CC BY) license.

To address lubricant depletion, it is necessary to design a new SLIPS surface that surpasses passive repellency and maintains performance during long-term use. A robust protective interface requires two key features: (1) intrinsic durability to resist the primary failure mode of lubricant depletion during long-term use, and (2) built-in, stimulus-responsive capability to actively maintain or recover functionality, such as through self-healing and on-demand property switching. This combination is particularly critical for applications like marine corrosion protection, where a coating must serve as a stable, long-term barrier while also withstanding inevitable mechanical damage. However, traditional self-healing strategies often address these requirements in isolation, leading to significant trade-offs. Extrinsic strategies (such as embedding microcapsules filled with healing agents) can achieve localized repair, but are constrained by limited reservoirs, preventing repeated repairs at the same location. They also often compromise the coating's initial mechanical integrity [11,12]. Intrinsic strategies based on reversible polymer networks, while capable of multiple repair cycles, are often constrained by slow self-healing kinetics, weak mechanical strength, and inadequate barrier performance against corrosive agents such as chloride ions in marine environments [13,14]. From our perspective, the fundamental bottleneck in current marine corrosion protection lies in the challenge of integrating long-term environmental barrier stability with rapid, active self-replenishing functionality without compromising the structural integrity of the metallic substrate.

To simultaneously meet these dual requirements, the most direct strategy is to replace the conventional liquid lubricant with a solid-state material serving as a multifunctional component. Phase-change materials (PCMs) are highly promising for this purpose. Specifically, paraffin wax is a suitable material owing to its combination of chemical stability, low cost, inherent hydrophobicity, and reversible thermally responsive phase transition. At ambient service temperatures, paraffin exists in a solid, immobile state, inherently eliminating the primary failure mechanisms of flow and evaporation that plague conventional SLIPS. This directly addresses the core durability challenge. Simultaneously, its reversible solid–liquid phase transition provides a built-in, responsive mechanism to achieve the desired intelligence: upon heating, the melting process enables rapid, volumetric self-healing of damage, while the resultant liquid film dramatically lowers surface adhesion, enabling on-demand, thermally switchable slipperiness. Furthermore, its chemical stability ensures resistance to degradation in aggressive environments such as seawater, while its hydrophobicity promotes compatibility with non-polar alkyl chains of modifier layers and enhances barrier properties against corrosive electrolytes. Its low cost and commercial availability further underscore its practical viability for large-scale engineering applications [15]. However, based on our expertise in interfacial engineering, we posit that the direct application of pure paraffin on metallic substrates is fundamentally unfeasible. This is due to two intrinsic, material-level defects that critically undermine interfacial stability. First, its non-polar, chemically inert nature results in inherently weak adhesion, relying solely on weak van der Waals forces with metal oxides [16]. Second, and more critically, paraffin undergoes a substantial volumetric contraction (typically 10–15%) upon solidification from the melt [17,18]. This inherent shrinkage generates significant internal tensile stress at the interface, which is the primary driver for crack formation and delamination in pure paraffin coatings [19]. Recognizing these challenges, previous research efforts have sought to mitigate them, providing valuable but partial solutions. Studies utilizing micro-arc oxidation (MAO) or chemical etching created porous structures to physically trap paraffin, improving short-term barrier properties [20–22]. Others developed polymer-paraffin composites, where the polymer matrix helped to buffer stress and enhance cohesion [23–26]. More recently, phase-change lubricant-infused surfaces have garnered significant attention for their smart, switchable wettability and sustainable anti-scaling properties [27,28]. While

these contributions demonstrated the potential of paraffin as a protective phase, they each addressed only one facet of the core material drawbacks in isolation. Porous structures improve physical entrapment but do not strengthen the weak chemical adhesion, leaving the interface vulnerable to debonding. Polymer composites may moderate stress but often introduce new weak boundaries prone to phase separation and can compromise the barrier's impermeability [29].

Therefore, a robust interface design must simultaneously satisfy the requirements of physical anchoring, chemical bonding, and stress dissipation. To achieve the required structures, various metallic surface modification technologies have been developed. While conventional methods like chemical etching and anodization can generate porous structures over large areas, they often rely on hazardous chemical effluents and lack precise control over the multiscale microstructures. Although femtosecond laser ablation technology still faces challenges in processing efficiency and cost when applied to large-area surfaces, it enables the precise fabrication defect-free hierarchical micro/nano-structures without chemical residues. Such structures are known to enhance capillary pressure and promote physical interlocking [30]. In addition, ongoing industrial advancements (e.g., high-power ultrafast lasers and multi-beam parallel processing) are expected to progressively enhanced address current limits [31]. Establishing a robust chemical bridge is equally critical. In surface functionalization strategies, interfacial mediators such as thiols and silanes are widely employed [32,33]. While thiols form robust coordinate bonds specifically with noble metals (e.g., Au, Ag, Cu), they are generally ineffective on highly passivated light metals like aluminum [34]. Silane coupling agents (e.g., OTES), however, are well-established for forming stable covalent bonds with the abundant hydroxyl groups on oxidized aluminum surfaces [35]. From economic and environmental perspectives, OTES was selected as a fluorine-free, commercially accessible, and practical alternative to the persistent, bioaccumulative perfluoroalkyl silanes traditionally used in slippery surfaces [36], effectively reducing surface energy and improving chemical compatibility. By combining these two technologies, it is possible to construct a structurally coherent interface that addresses the intrinsic limitations of solid phase-change lubricants.

In this work, to fundamentally address the intrinsic issues of rapid lubricant depletion and weak interfacial adhesion, we propose a laser-engineered hierarchical architecture, termed HPS-P (Hierarchical Porous Structure-Paraffin). Unlike conventional liquid-infused surfaces or simple solid paraffin coatings, the originality of this work lies in a synergistic "dual-locking" mechanism that integrates multi-scale physical interlocking with chemical bridging. Specifically, we fabricated a hierarchical porous structure (HPS) featuring interconnected micro-grooves and nano-clusters on an aluminum alloy to serve as reservoirs for accommodating volume shrinkage and as capillary anchors. Subsequently, an OTES layer was covalently grafted onto the HPS to strengthen the interfacial adhesion with the infused paraffin. This integrated design endows the resulting HPS-P coating with three specific functionalities: (1) on-demand, thermally switchable slipperiness; (2) rapid (~100 s) thermal self-healing of mechanical damage; and (3) superior corrosion protection, with the corrosion current density reduced by six orders of magnitude relative to the bare aluminum alloy. By demonstrating that a multi-scale interfacial architecture can resolve the durability constraints of conventional liquid-infused surfaces, this work provides an effective structural design strategy for durable, thermally responsive protective coatings in harsh engineering environments.

2. Materials and Methods

2.1. Materials

The 7075 aluminum alloy with a composition (5.95-Zn, 2.27-Mg, 1.45-Cu, 0.28-Fe, 0.18-Mn, 0.13-Si, 0.20-Cr and Bal-Al in wt. %) was cut into 20 mm × 20 mm × 2 mm as the substrate material. Chemical reagents, including anhydrous ethanol (AR, ≥99.0%), Octyltriethoxysilane (OTES, CAS: 2943-75-1, 97%), and paraffin wax (m.p. 58 °C) were used for the preparation of the coating. The pH testing used standardized aqueous solutions of hydrochloric acid (HCl, AR, 0.1 mol/L) and sodium hydroxide (NaOH, AR, 0.1 mol/L). To prevent degradation by atmospheric carbon dioxide, the NaOH solution was kept tightly sealed and dispensed immediately prior to use. The solid sodium chloride (NaCl, AR, ≥99.5%) was involved in the electrochemical testing. The OTES and other reagents were bought from Shanghai Yien Chemical Technology Co., Ltd. (Shanghai, China) and Sinopharm Chemical Reagent Co., Ltd. (Shanghai, China), respectively, and the deionized water was self-made in the laboratory.

2.2. Preparation of HPS by Femtosecond Laser Ablation

Before being laser processed, the aluminum alloy substrate needed to be polished by 800# and 2000# silicon carbide sandpaper to remove its oxide layer firstly, then ultrasonically cleaned in anhydrous ethanol and deionized water for 5 min to remove its surface contaminants, finally dried with hot air and set aside for later use.

The HPS was obtained after the surface of aluminum alloy sample was processed in the air by a femtosecond laser processing system (Tangerine HP, Amplitude Systèmes, Bordeaux, France) that is shown in Figure S1. The fiber femtosecond laser generated a Gaussian pulsed beam with a wavelength of 1030 nm, a repetition rate (f) of 175 kHz and a pulse duration of 250 fs. The laser beam passed successively through the half-wave plate, beam expander, reflector, and aperture, then entered the scanning galvanometer (IntelliSCAN III14, SCANLAB, Pulheim, Germany), and finally focused on the sample on the translation stage through a F-theta objective with a focal length of 160 mm. The spot diameter (ω_0) of the sample surface is about 30 μm. The HPS was obtained by processing in horizontal and vertical directions using a computer-controlled line-by-line scanning mode. The laser scanning speed and line pitch were set to 50 mm/s and 50 μm, respectively. In order to adjust the microstructure, the output powers were set to 1.45 W, 2.42 W and 3.56 W, and the corresponding single-pulse energies (E) were, respectively, 8.29 μJ, 13.83 μJ, and 20.34 μJ calculated by $E = P/f$. The treated surfaces were named as HPS-1, HPS-2 and HPS-3, corresponding to the laser peak fluence of 2.34 J/cm^2, 3.91 J/cm^2, 5.76 J/cm^2 calculated by $F = 8E/(\pi\omega_0{}^2)$.

2.3. Preparation of HPS-S Coatings and HPS-P Coatings

Figure 1a shows the preparation processes of HPS-S coatings and HPS-P coatings. HPS-S coatings were prepared by OTES's modification to femtosecond laser-ablated HPS, which experienced four steps. Firstly, 1 mL of OTES and 98 mL of anhydrous ethanol were measured and put into a beaker, 0.5 mL of deionized water was instilled drop by drop under magnetic stirring, and 2–3 drops of 0.1 M hydrochloric acid was added as a hydrolysis catalyst. Acid-catalyzed hydrolysis was deliberately chosen over base catalysis because acidic conditions promote the rapid hydrolysis of ethoxy groups into reactive silanols while maintaining a low rate of self-condensation, ensuring uniform surface grafting rather than premature agglomeration. Secondly, the OTES mixed solution was placed in a constant temperature environment of 25 °C and stirred continuously at a speed of 500 rpm for 30 min. Then, HPS samples were left to stand in the OTES mixed solution for 1 h. Finally, those

samples were transferred to a forced convection drying oven at 110 °C and heat-treated for 10 min to obtain HPS-S coatings.

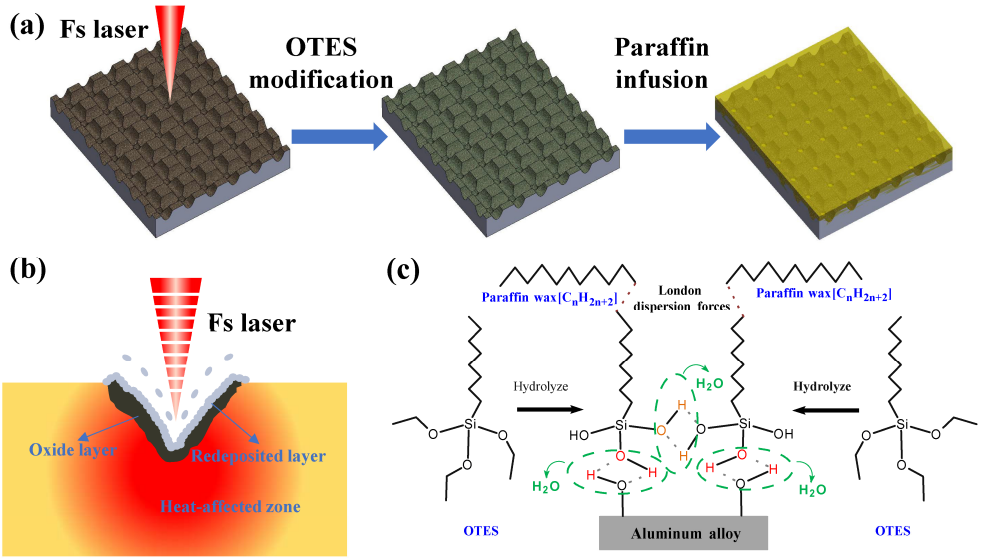


Figure 1. (**a**) Fabrication process of HPS-P coating. (**b**) Schematic diagram of femtosecond laser ablation. (**c**) Schematic diagram of paraffin, OTES, combined with aluminum alloy.

In this research, HPS-P coatings were processed by a paraffin thermal impregnation method. Specifically, HPS-S coating samples were vertically immersed in the molten paraffin at 110 °C and maintained in a fully submerged state for 60 s. Those samples were then withdrawn at a constant speed and immediately placed horizontally under the ambient temperature. After natural cooling and solidification, a dense and uniform paraffin layer was formed and HPS-P coatings were produced finally.

Figure 1c schematically illustrates the interaction mechanism of OTES and the paraffin with the aluminum alloy surface. The silanization of the aluminum alloy surface with OTES primarily involved three key steps. The first one was hydrolysis reaction: the triethoxy group of OTES was hydrolyzed under the action of water molecules to generate the silanol (–Si–OH). Then came the condensation reaction: the silanol generated by hydrolysis reacted with the hydroxyl group on the surface of the aluminum alloy (–OH) to form a strong covalent bond. The last one was the self-condensation cross-linking: the multimolecules condensed with each other to form a Si–O–Si network structure. An organic-inorganic hybrid film containing Si–O–Al bonds and hydrophobic octyl chains ($–C_8H_{17}$) was eventually formed on the surface of the aluminum alloy. The long alkyl hydrophobic tail of OTES interacted with the paraffin through London dispersion forces, which resulted in significant adhesion between both [14]. The chemical equations for the silanization reactions are as follows:

$$\text{Hydrolysis: } CH_3(CH_2)_7Si(OCH_2CH_3)_3 + 3H_2O \xrightarrow{H^+} CH_3(CH_2)_7Si(OH)_3 + 3CH_3CH_2OH$$

$$\text{Condensation with substrate: } CH_3(CH_2)_7Si(OH)_3 + \text{Al-OH} \rightarrow CH_3(CH_2)_7\text{Si-O-Al} + H_2O$$

$$\text{Self-condensation: } 2CH_3(CH_2)_7Si(OH)_3 \rightarrow CH_3(CH_2)_7\text{Si-O-Si}(OH)_2(CH_2)_7CH_3 + H_2O$$

2.4. Characterization

The sample morphologies were characterized by the field scanning electron microscopy (SEM, CLARA, TESCAN, Brno, Czech Republic). The chemical compositions were characterized by the energy dispersive spectrum (EDS, Xplore30, Oxford, UK) and the X-ray photoelectron spectroscopy (XPS, Axis Supra+, Kratos, Manchester, UK). The

static contact angle (CA) and dynamic sliding angle (SA) were measured by a contact angle meter (JC2000C1, Powereach, Shanghai, China) with a 6.5 μL droplet of deionized water. At least five different surface positions were measured for each sample.

The corrosion resistance was characterized by the electrochemical workstation (Interface 1010E, Gamry, Philly, PA, USA). Those samples were placed in the plate corrosion electrolytic cell (Gaossunion, Wuhan, China) with 3.5 wt.% NaCl solution at room temperature for test. A saturated calomel electrode (SCE), a 20 mm × 20 mm Pt mesh and the sample were used as the reference electrode, the counter electrode and the working electrode (with 1 cm^2 circular exposed area), respectively. Firstly, the sample was submerged in NaCl solution for 1 h to obtain relatively stable open circuit potential. The electrochemical impedance spectra (EIS) curves were obtained at the open circuit potential among the frequencies ranging from 10^5 Hz to 0.2 Hz by applying a perturbation amplitude voltage of 10 mV. To eliminate electromagnetic interference during the high-impedance measurements, the electrolytic cell was housed within a grounded Faraday cage. The polarization curves were obtained by scanning from −0.5 V to 1.5 V with respect to the open circuit potential at a rate of 1 mV/s.

3. Results and Discussion

3.1. Fabrication and Optimization of Hierarchical Porous Structures

To create a durable interface capable of permanently locking a solid-phase lubricant, we engineered a synergistic architecture that integrates a hierarchical physical structure with robust interfacial chemistry. The foundation of this architecture is a hierarchical porous structure (HPS) fabricated on the aluminum alloy surface via femtosecond laser ablation. The femtosecond laser's ultrashort pulse duration (250 fs), which is below the electron-phonon relaxation time, drives a "cold ablation" mechanism. This minimizes the heat-affected zone (HAZ) and avoids thermal residual stresses or micro-cracks, thereby maintaining the substrate's inherent mechanical stability and long-term reliability. The formation mechanism, illustrated schematically in Figure 1b, is initiated by the intense interaction between high-energy laser pulses and the aluminum alloy surface. Concurrently, while a thin native oxide film forms spontaneously on aluminum in air, the instantaneous high-temperature plasma generated at the laser focal point induces extreme localized oxidation of the ejected material. This results in the redeposition of structurally distinct, dense nano-scale oxide clusters that cover the sample. A line-by-line scanning strategy in both horizontal and vertical directions is then employed: the laser ablation forms micro-scale grooves along each scanned line, and where these lines intersect, micro-pores are generated. This systematic approach ultimately fabricates a uniform HPS across the sample surface.

Figure 2 displays the morphologies of HPS fabricated on aluminum alloy using three different parameters of femtosecond laser. As shown in Figure 2a, the HPS-1 surface is characterized by a periodic array of micro-protrusions. Each protrusion is surrounded by four micro-grooves, with micro-pores present between these grooves. The magnified SEM image (Figure 2d) reveals that the surfaces of these micro-protrusions are covered with numerous irregularly shaped sub-micron clusters. Each sub-micron cluster is formed by the redeposition of tens of nanometers nanoparticles (Figure 2a inset, indicated by the yellow dashed box in Figure 2d). Similarly, HPS-2 and HPS-3 also consist of micro-protrusions covered with sub-micron clusters and nanoparticles (Figure 2b–f). Compared with HPS-1, HPS-2 and HPS-3 exhibit progressively deeper micro-grooves and micro-pores. To quantitatively determine these topographical differences, 3D surface topography was measured using a 3D optical profilometer (Figure S2). Based on the raw spatial coordinate data, the robust surface porosities were calculated to be 24.52%, 31.97%, and 36.56% for

HPS-1, HPS-2, and HPS-3, respectively (the detailed calculation methodology is provided in the Supplementary Materials). These quantitative results confirm that higher laser peak fluences lead to greater ablation depths and progressively larger capacities for paraffin storage. Consequently, HPS-3 possesses the largest pore volume and the most developed micro/nanostructures. Concurrently, the coverage area of sub-micron clusters on the micro-protrusions of HPS-2 and HPS-3 also shows a sequential increase, implying an enhanced ability to adsorb more liquid paraffin via capillary action. The EDS elemental analysis (Figure 2d–f and full spectra in Figure S3) confirms the presence of Al, O, Zn, and Mg. Specifically, the atomic ratios of oxygen increase progressively from HPS-1 (28.4%) to HPS-2 (34.3%) and HPS-3 (37.5%). This quantitative increase confirms that higher laser fluences promote more intense localized oxidation, aligning with the distribution of sub-micron clusters.

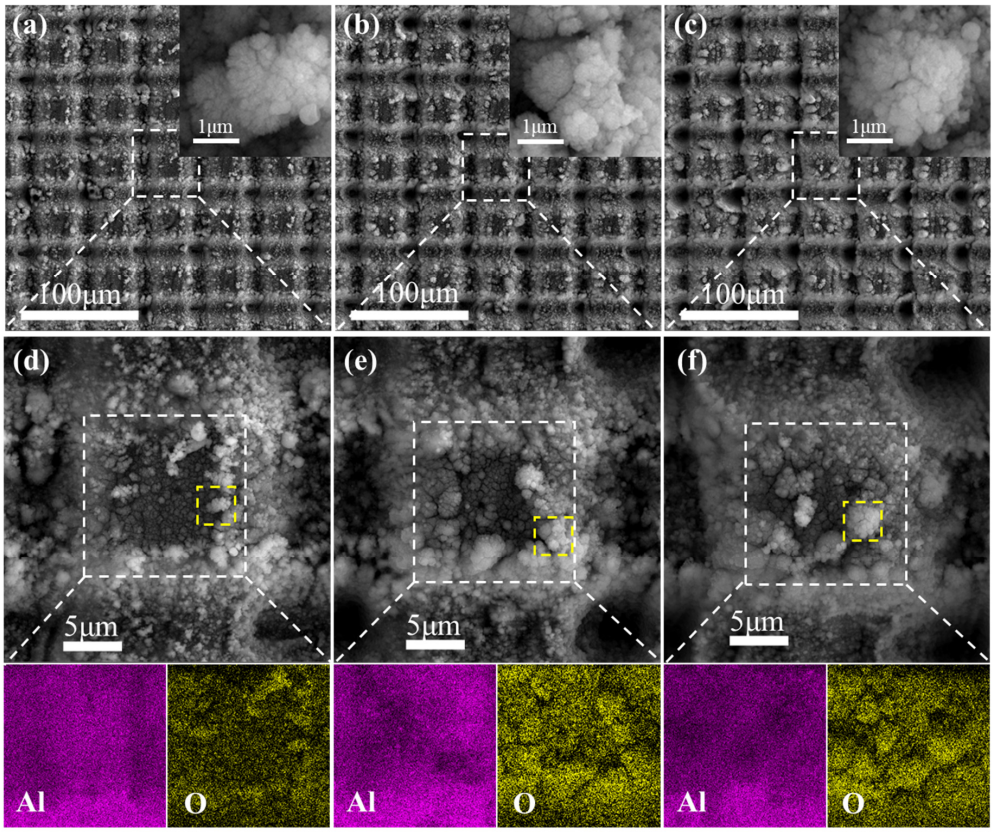


Figure 2. The surface morphology at different laser parameters. (**a**) HPS-1, (**b**) HPS-2, (**c**) HPS-3. The high-magnification insets in the upper right corners correspond to the regions marked by the yellow dashed boxes in (**d**–**f**). (**d**–**f**) the corresponding high magnification and EDS diagrams of (**a**–**c**), respectively.

As shown in Figure 2, HPS-3 possesses the largest pore volume and the most developed micro/nanostructures. These features enable it to not only accommodate a greater amount of paraffin but also to enhance the overall coating integrity through several mechanisms. Specifically, the surface micro-pores and micro-grooves act as reservoirs for paraffin and provide physical anchoring points, thereby strengthening the mechanical interlocking between the paraffin and the substrate. Furthermore, the micro-grooves function as channels for liquid flow; during paraffin solidification, they facilitate the capillary-driven transport of unsolidified liquid paraffin to regions experiencing shrinkage, thus mitigating crack formation induced by contraction stress. Concurrently, the micro-protrusions serve to support the solidified paraffin structure, effectively dispersing solidification stresses. The presence of these surface oxides also provides abundant hydroxyl (−OH) sites crucial

for the subsequent adsorption and anchoring of OTES molecules. Therefore, HPS-3 was selected as the optimal structure for all subsequent investigations.

3.2. Morphology and Composition of the HPS-P Coating

Based on the optimized HPS-3 structure, the final HPS-P coating was prepared via silanization and subsequent paraffin impregnation. This silanization step was designed to reduce the surface energy of the HPS, rendering it non-polar (hereafter referred to as HPS-S) and thereby promoting favorable wetting and interaction with the paraffin. With this enhanced surface energy compatibility, molten paraffin (at 110 °C) could readily infiltrate the HPS, driven by capillary and dispersive forces, to form the final HPS-P coating. As shown in Figure 3a, after impregnation treatment, the surface that initially possessed a porous and layered structure transformed into a dense, uniform, and macroscopically smooth coating. The surface is largely free of the cracks or pores that commonly undermine simple paraffin coatings. When injected paraffin cools from 110 °C to room temperature, it typically undergoes a 10–15% volumetric shrinkage, generating significant internal tensile stresses. However, the absence of macroscopic defects indicates that the underlying HPS effectively mitigates this thermally induced stress associated with solidification by facilitating capillary-driven refilling and stress dispersion.

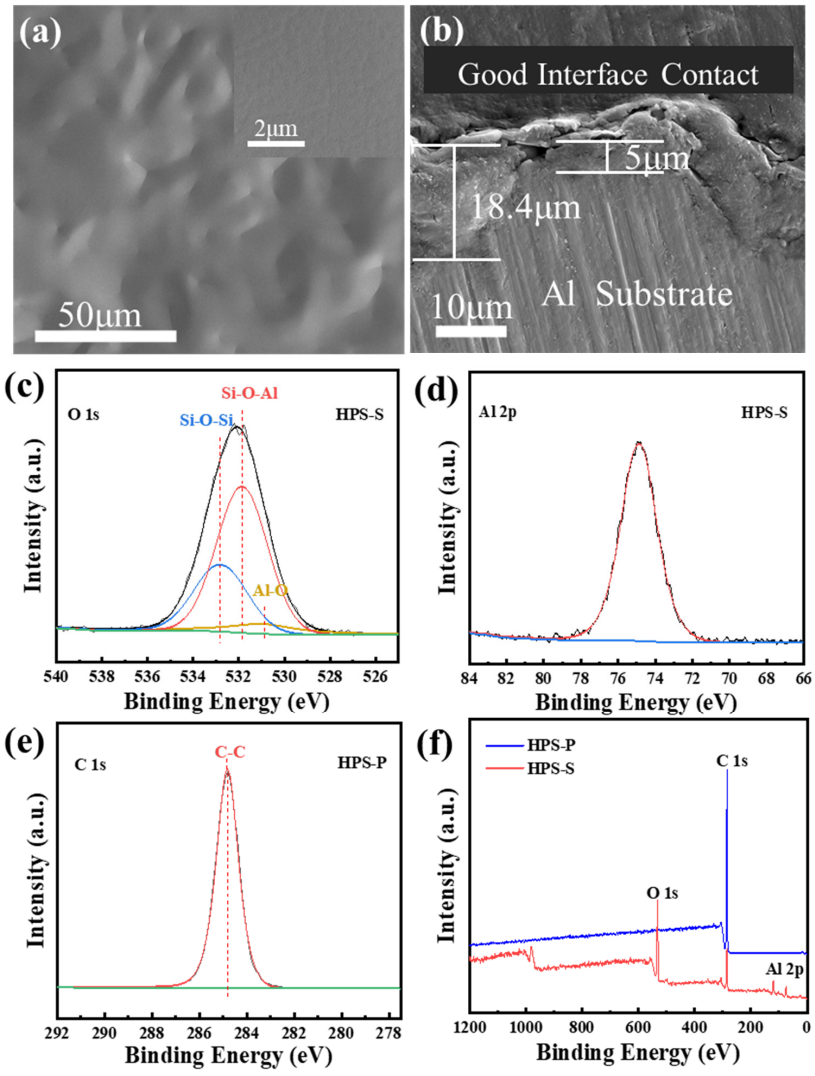


Figure 3. (**a**) The surface morphology of HPS-P coating. (**b**) Cross-sectional SEM images of HPS-P coating. (**c**–**f**) XPS spectra of the HPS-S and the HPS-P: (**c**) O 1 s of HPS-S; (**d**) Al 2 p of HPS-S; (**e**) C 1 s of HPS-P; (**f**) XPS survey spectra.

Figure 3b shows that the HPS-P coating exhibits continuous conformal contact with physical interlocking, virtually eliminates observable interfacial voids or delamination from the cross-sectional view. The paraffin layer is seen to conform to and fully fills to the laser-etched topography, having fully penetrated and filled the micro-grooves. This infiltration results in a substantial local thickness of approximately 18.4 μm within these reservoirs, contrasting with a thickness of about 5 μm over the protrusions. This indicates that the solidified paraffin is mechanically anchored within the multiscale HPS composite surface.

To probe the interfacial chemical evolution, X-ray photoelectron spectroscopy (XPS) was employed (Figure 3c–f). Figure 3c presents the deconvoluted O 1 s spectrum of the silanized surface (HPS-S). The peak fits into three distinct components: Al–O (~531.0 eV) from the substrate, Si–O–Si (~532.8 eV) from the silane network, and Si–O–Al (~531.9 eV). The emergence of the Si–O–Al bond provides direct evidence that the OTES molecules are covalently grafted onto the aluminum substrate via condensation reactions, establishing a robust chemical bridge.

Upon paraffin infusion, the surface chemistry undergoes a fundamental transition. The C 1 s high-resolution spectrum of HPS-P (Figure 3e) is dominated by a sharp peak at 284.8 eV, corresponding to the C–C/C–H bonds of the paraffin chains. Further compositional evidence for the coating's integrity is found in the survey spectra comparison (Figure 3f). While the HPS-S spectrum (red line) clearly displays Al 2p and Al 2s peaks from the substrate (with atomic ratios of C 42.1 ± 1.42%, O 39.5 ± 1.14%, and Al 18.4 ± 0.98%), these metallic signals completely disappear in the HPS-P spectrum (C 99.7 ± 0.56%, O 0.0 ± 0.42%, Al 0.2 ± 0.37%). Since the sampling depth of XPS is typically <10 nm, this "signal masking" effect confirms that the paraffin has formed a continuous, defect-free layer that is thick enough to fully encapsulate the underlying substrate. This complete coverage isolates the metal from the environment, laying the chemical foundation for the superior corrosion resistance discussed later.

3.3. Visualization of Self-Healing

Next, we investigated the active self-replenishing capability of the HPS-P architecture. This capability is key to the coating's ability to cope with mechanical damage and achieve long-term protection. To visualize this, the thermal healing dynamics of a 130 μm wide scratch were monitored in situ via optical microscopy (Figure 4a–f; Video S1). Upon heating the scratched sample at 2 °C/s, a distinct solid-to-liquid transition was observed. The paraffin adjacent to the defect melted and initiated an inward flow (Figure 4b), with the molten front propagating radially outward (Figure 4c). At the fully molten stage, the coating became optically transparent, exposing the underlying HPS framework (Figure 4d), which confirms the high fluidity of the lubricant reservoir. Following a brief 5 s dwell and subsequent cooling, the paraffin recrystallized to form a continuous barrier (Figure 4e), effectively erasing the original scratch (Figure 4f). The emergence of subtle surface texturing post-solidification is consistent with the release of crystallization stresses, confirming that the physical barrier remained intact.

Figure 4g elucidates the mechanism underpinning this rapid repair. The HPS architecture functions as a thermally responsive reservoir where the phase change in the stored paraffin is thermally triggered. Driven by the minimization of surface energy and strong capillary forces induced by the laser-engineered nanostructures, the low-viscosity molten paraffin efficiently replenishes the defect site. The entire healing cycle (encompassing heating, melting, refilling, and resolidification) is accomplished within 100 s. Unlike static barriers, our coating achieves durability through a dynamic mechanism. We term this the 'active self-replenishing capability', which underpins the macroscopic self-healing properties observed. As highlighted in the comparative analysis with existing literature (Figure 4h), this

kinetics, supported by the physical reservoir, is significantly superior to many reported intrinsic self-healing systems [13,24,37–49]. It is worth noting that the coatings compared herein encompass diverse chemical natures, physical properties, and preparation methods. Rather than equating the underlying micro-mechanisms, this comparison benchmarks macroscopic healing time (a critical parameter for engineering applications) to substantiate the effectiveness of the hierarchical locking strategy in mitigating mechanical damage.

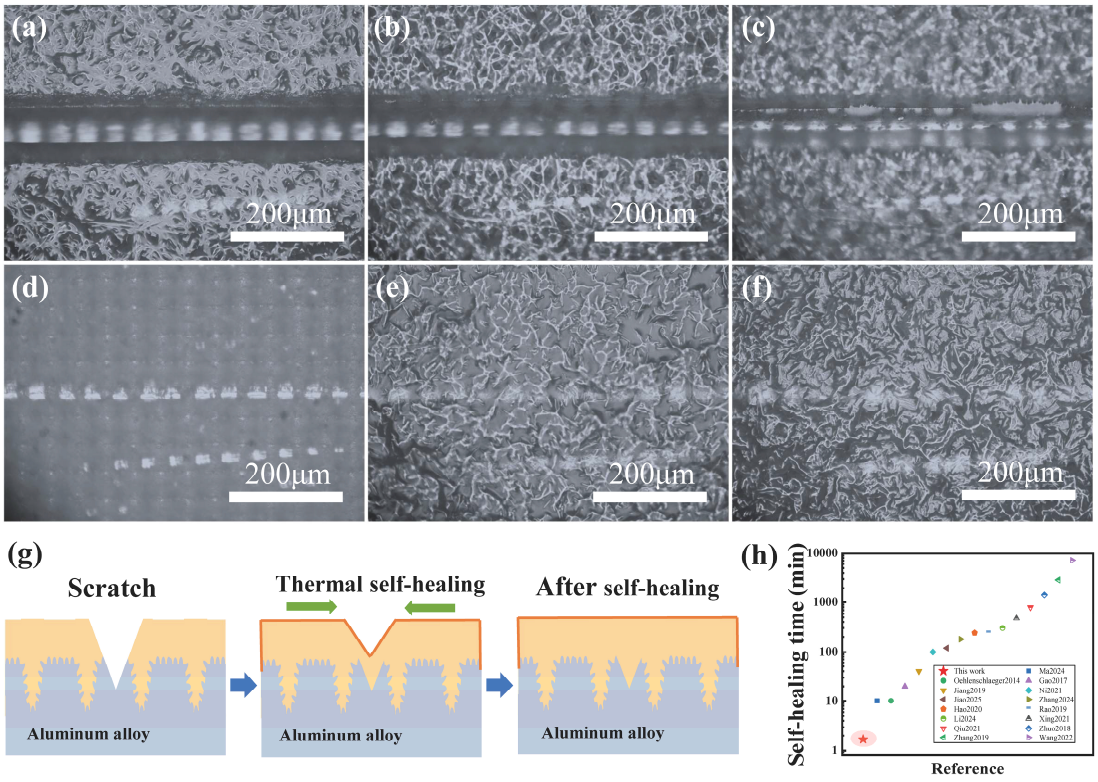


Figure 4. (**a**–**f**) Optical microscopic images of HPS-P coating during self-healing process. (**g**) Schematic diagram of the self-healing mechanism of the coating. (**h**) Comparison of self-healing time of coatings reported in previous studies [13,24,37–49].

3.4. Stability and Thermally Switchable Wettability

To validate the reliability of the HPS-P coating for practical applications, we first evaluated its wetting behavior and environmental robustness. Figure 5a shows the untreated sample following chemical modification with OTES exhibited a CA of 93.2° ± 2°, indicative of a typically hydrophobic surface (CA > 90°). The CA of HPS-S coating was significantly increased to 154.7° ± 0.7°, and the SA was as low as 1.2° ± 0.7° (Figure S5), reaching the superhydrophobic standard (CA > 150° and SA < 10°). This transition is mainly attributed to the highly rough surface induced by femtosecond laser ablation, which traps air pockets and forms a Cassie–Baxter state. The locked air layer not only effectively blocks the penetration of corrosive media but also reduces the actual solid–liquid contact area to 9.93%. After impregnating the HPS-S with liquid paraffin, the synergistic effect of capillary forces and van der Waals forces drives the liquid paraffin to displace the trapped air within the porous structure. At this time, the CA of HPS-P coating decreased to 107.2° ± 2°. Although it lost superhydrophobicity, it still maintained hydrophobicity. This indicates that the surface of HPS-P transforms to the fully wet Wenzel state, and the paraffin filling has completely covered the HPS.

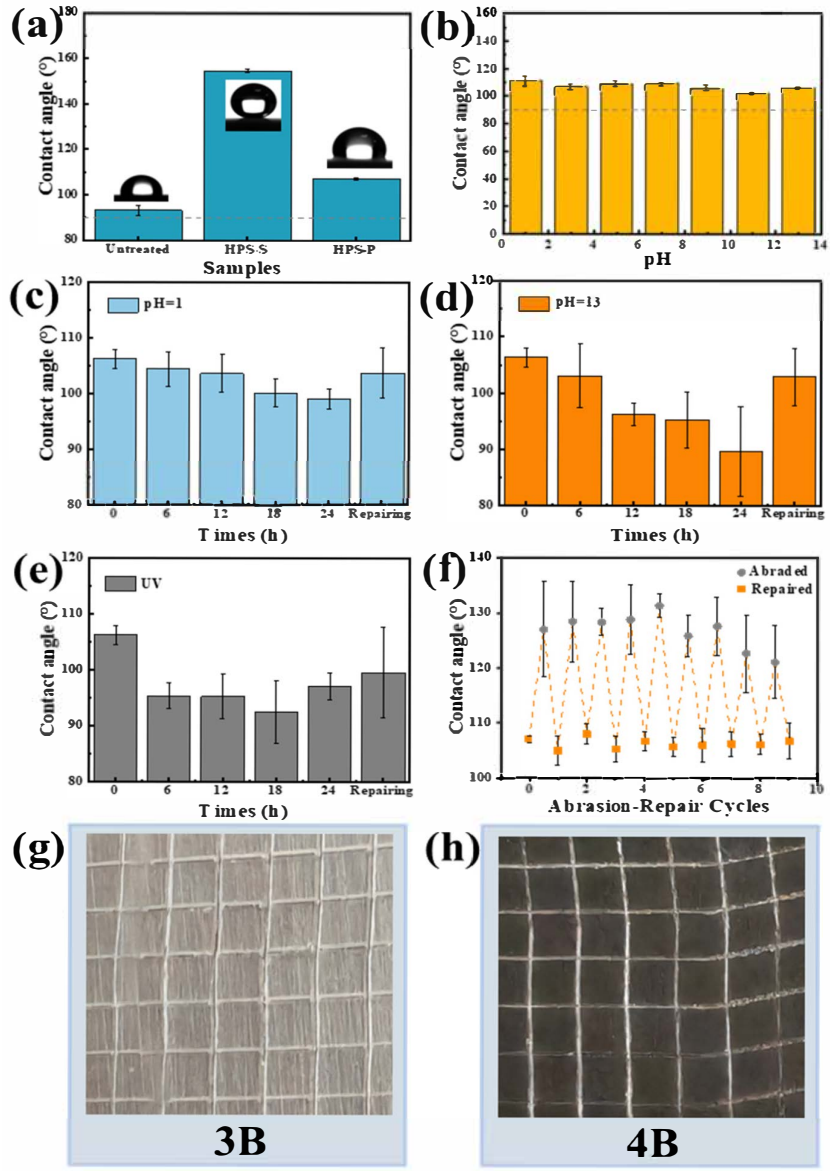


Figure 5. (**a**) The CAs of Untreated sample, HPS-S and HPS-P. (**b**) The CAs with different pH value of HPS-P. (**c**,**d**) The CAs of the HPS-P in hydrochloric acid (pH = 1) and sodium hydroxide solution (pH = 13). (**e**) The CAs of the HPS-P under UV irradiation. (**f**) The CAs of the HPS-P with abrasion-repair cycle test. (**g**) Adhesion testing of the control sample. (**h**) Adhesion testing of the HPS-P coating.

The solid–liquid contact ratio of superhydrophobic surfaces can be calculated by the Cassie–Baxter model [50]:

$$cos\theta_{CB} = f_s(cos\theta_0 + 1) - 1 \quad (1)$$

where $cos\theta_{CB}$ (154.7°) is the CA of HPS-S coating (the apparent contact angle), and θ_0 is the intrinsic contact angle on smooth surface (93.2° for Untreated sample). The solid–liquid contact ratio f_s is calculated to be 9.93% by Equation (1).

The stability of coatings is crucial to the actual durability of the metal surface. To evaluate the chemical stability of the HPS-P coatings, the CAs of different pH values were measured. As shown in Figure 5b, all CAs remained above 100° over the pH range of 1 to 13. This indicates that the HPS-P coating maintains its hydrophobicity over a wide pH range, suggesting good initial chemical stability against brief exposure to acidic and alkaline environments.

To further evaluate the long-term chemical stability, the HPS-P samples were immersed in the hydrochloric acid solution (pH = 1), the sodium hydroxide solution (pH = 13), and UV irradiation for 24 h, respectively. The static CAs of the coatings were measured during the immersion period. As shown in Figure 5c, the water CA decreased slightly to 99.1° after 24 h of immersion in an acidic solution (pH = 1). This suggests that the paraffin coating still has strong chemical resistance in a long-term acidic environment. As shown in Figure 5d, after 24 h of immersion in an alkaline solution (pH = 13), the CA decreased to 89°, and the sample lost its hydrophobicity. Nevertheless, the sample maintained its hydrophobicity for up to 18 h of immersion in the alkaline solution (pH = 13). This indicates that while the paraffin coating offers substantial resistance to alkaline environment for an extended period (up to 18 h), prolonged exposure (24 h) leads to surface degradation and loss of hydrophobicity. This pronounced decrease in hydrophobicity is primarily attributed to the prolonged interaction between the highly concentrated basic medium (pH = 13) and the outermost solid paraffin layer. Extended exposure induces physical erosion and surface micro-emulsification of the paraffin wax, generating macroscopic surface defects that compromise the original water-repellent topography. As shown in Figure 5e, after 24 h of exposure to a UV lamp (7 W, 395 nm), the CA remained above 90°, maintaining its hydrophobicity. This demonstrates that the HPS-P coating can withstand chemical degradation damage caused by long-term UV exposure.

After 24 h of tests under acid, alkali, and UV irradiation, the HPS-P coatings were heated on a hot plate at 110 °C for 30 s, followed by natural cooling. The CAs recovered to 103.8°, 103.0°, and 100.2°, respectively. This recovery is due to the melting and reflowing of paraffin upon heating, which repairs the surface modification or degradation caused by acid/alkali exposure or UV irradiation. This demonstrates that the HPS-P coatings have excellent thermal self-healing property even after exposure to harsh chemical environments or UV radiation.

The mechanical durability of the HPS-P coating was evaluated by a sandpaper abrasion test. In the abrasion test, the HPS-P sample was pressed face down onto 800# sandpaper under a 200 g load. Subsequently, the sample was moved horizontally for 5 cm at a speed of 1 cm/s, completing one abrasion. Afterwards, the sample was placed on a hot plate at 110 °C for 30 s, followed by natural cooling. This entire process was defined as one test cycle. The initial water CA of the HPS-P coating was 107.2°. Figure 5f shows the CA changes during the sandpaper abrasion test. After the first 5 cm abrasion pass, the CA of the HPS-P coating increased to 130.0°. This phenomenon is attributed to the roughening of the paraffin surface caused by abrasion. After thermal repair, the CA of HPS-P coating recovered to 105.2°, approaching its initial hydrophobicity. Notably, after 9 abrasion-repair cycles, the CA of the HPS-P coating after thermal repair could still be maintained at 106.9°, consistently demonstrating stable hydrophobicity. Although repeated abrasion inevitably leads to some paraffin loss from the HPS-P coating surface, its unique porous structure is capable of storing paraffin. During the thermal repair process, this stored paraffin flows upon heating to refill the abraded areas, effectively restoring the integrity and hydrophobicity of the coating surface. This indicates that the HPS-P coating, by virtue of its excellent thermal self-healing property, can maintain its critical water-repellent performance even after repeated mechanical damage, thus exhibiting good mechanical durability and damage tolerance.

Adhesion testing (ASTM D3359 [51]) further elucidates the mechanism behind this durability. The control sample (prepared without laser ablation, consisting only of paraffin infused on flat silanized aluminum) achieved a moderate adhesion grade of 3B (Figure 5g), indicating that while chemical bonding contributes to stability, its edges remain susceptible to delamination propagation. In contrast, the HPS-P coating achieved an enhanced 4B rating (Figure 5h) with minimal peel area (<5%). This improvement validates the "syn-

ergistic locking" mechanism: the silane interface provides foundational chemical affinity, while laser-formed microanchors physically constrain peel propagation, ensuring coating integrity in dynamic environments.

The physical basis for the rapid self-healing observed in the previous section lies in the phase-change nature of the lubricant, which concurrently endows the surface with unique 'thermally switchable adhesion'. At ambient temperature, the solid HPS-P surface exhibits a 'pinning' state (Figure 6a–c): water droplets adhere strongly without rolling off, even at extreme tilt angles of 90° or 180°. This high-adhesion superhydrophobicity is attributed to the Wenzel regime induced by the roughness of the solidified paraffin, where water penetrates the structural asperities, generating strong van der Waals forces and capillary adhesion. However, upon heating above the melting point, the surface instantly switches to a 'slippery' state (Figure 6d): the solid paraffin melts to form a smooth liquid film, masking the surface roughness and eliminating the pinning effect. Consequently, droplets slide off easily at tilt angles < 10°. This smart transition from a 'high-adhesion solid' to a 'super-slippery liquid' state not only enables on-demand droplet manipulation but also mechanistically corroborates the high mobility of liquid paraffin within the HPS network, which is the prerequisite for the rapid active self-replenishing capability.

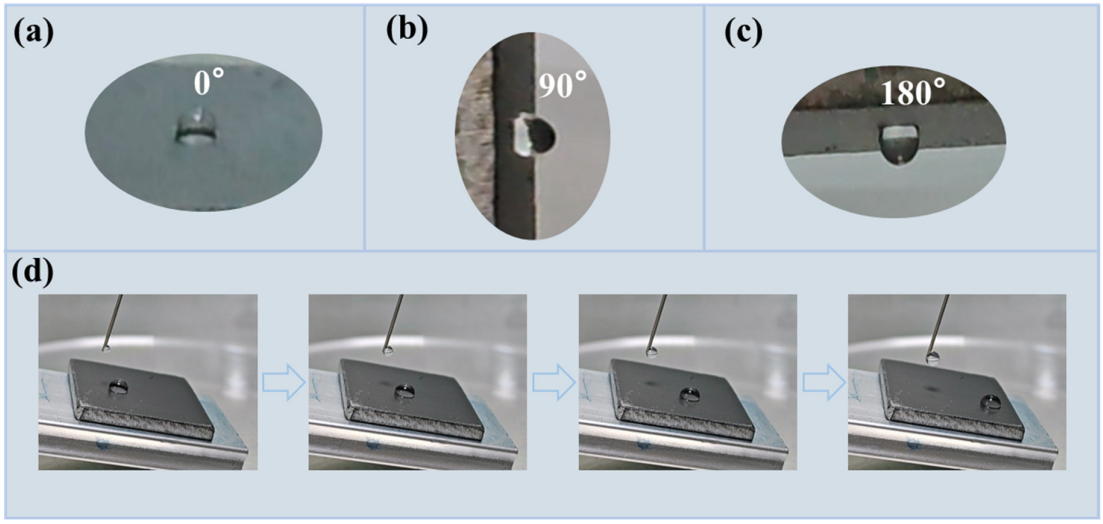


Figure 6. (**a**–**c**) Contact angle diagrams for HPS-P at room temperature with tilt angles of 0°, 90°, and 180°. (**d**) Sliding diagram of droplets on an inclined HPS-P surface after heating.

3.5. Anti-Corrosion Performance

The anti-corrosion performance is a critical indicator for evaluating the practical reliability of the HPS-P coating. We first investigated the corrosion protection behavior via potentiodynamic polarization curves in 3.5 wt.% NaCl solution (Figure 7a). The E_{corr} of Untreated sample, HPS-S sample and HPS-P sample are −0.682 V, −0.765 V, −0.665 V, respectively. Compared to the Untreated sample, the I_{corr} of HPS-S sample significantly decreases from 5.69×10^{-6} A/cm^2 to 4.50×10^{-9} A/cm^2, approximately by three orders of magnitude. The reduction in I_{corr} is much greater than the surface air–liquid contact ratio (90.07%), indicating that in addition to the air layer of HPS-S reducing the corrosion rate, the oxide layer of femtosecond laser ablation also protects aluminum alloy from corrosion. The I_{corr} of HPS-P further decreases to 2.32×10^{-12} A/cm^2, which is ca.6 and ca.3 orders of magnitude lower than that of Untreated sample and HPS-S, respectively. This indicates that the dense paraffin layer effectively blocks the contact between the corrosive medium and the metal substrate, thereby significantly inhibiting corrosion reactions.

To further investigate the corrosion resistance of the coatings, the electrochemical impedance spectra (EIS) were tested after immersion in 3.5 wt.% NaCl solution for 1 h. As shown in Figure 7b, the semicircle diameters of the Untreated sample, HPS-S and HPS-P in the Nyquist plots are several kΩ·cm^2, MΩ·cm^2 and GΩ·cm^2, respectively. The Bode phase angle and Bode impedance plots were shown in Figure 7c, d. The phase angle maxima and phase angle aperture were related with the capacitive behavior, the observed higher phase angle and phase angle aperture for HPS-S than the Untreated sample indicated better corrosion resistance. From high to low frequencies, the phase angle of HPS-P is close to −90°, which means that corrosive ions are unable to penetrate the interface between the substrate and the paraffin coating, showing excellent corrosion protection.

The low frequency impedance modulus $|Z|$ can be used to semi-quantitatively evaluate anti-corrosion performance, and a larger $|Z|$ indicates better performance. Figure 7d shows that HPS-P coating exhibited a significant increase in impedance modulus compared to Untreated sample and HPS-S, the highest $|Z|$ of 1.38 × 10^{10} Ω·cm^2 was measured for HPS-P coating and the best barrier performance was provided. To further obtain the impedance parameters, the electrochemical behavior of the sample immersed in solution can be simulated by an equivalent circuit. Figure 7h shows that the equivalent circuit of HPS-P is R_s (Q_f (R_{ct})). The equivalent circuits for the Untreated sample and HPS-S are shown in Figure S6, corresponding to R_s (Q_f (R_f ($Q_{dl}R_{ct}$))) and R_s (Q_f (R_f (Q_{dl} ($R_{ct}W$)))), respectively. In the equivalent circuits, R_s is the 3.5 wt.% NaCl solution resistance; R_f and R_{ct} represent the resistance of the anti-corrosion layer (corrosion product, air) and the charge-transfer resistance; Q_f and Q_{dl} are the constant phase elements modeling capacitance of the anti-corrosion layer and double electrode layer; W stands for the Warburg resistance. Here, the constant phase element (CPE) instead of pure capacitance was used to represent the non-ideal capacitor, which can be calculated by the Brug equation [52]:

$$CPE = \left(Y_0 R^{1-n}\right)^{\frac{1}{n}} \quad (2)$$

where Y_0 stands for frequency-independent real constant, n presents the constant phase element exponent ($0 < n \leq 1$, n = 1 means CPE is "pure capacitance"), and R is the resistance of the specific group. The electrical impedance of CPE can be calculated by Equation (3), Where j is an imaginary unit and ω is an angular frequency ($\omega = 2\pi f$).

$$Z_{CPE} = \frac{1}{Y_0(j\omega)^n} \quad (3)$$

Table 1 shows the fitted EIS results of different samples in 3.5 wt.% NaCl solution based on equivalent circuit models. The equivalent circuit parameters, including R_s and R_{ct}, were numerically optimized and fitted using a Levenberg–Marquardt fitting algorithm, with the goodness of fit (χ^2) strictly maintained below 10^{-3} to ensure data reliability. The coating capacitance (C_f) is an effective indicator of water absorption of coatings. The C_f of HPS-P was calculated to be a value of 5.65 × 10^{-5} μF·cm^{-2}, which was much lower than that of HPS-S (1.21 × 10^{-3} μF·cm^{-2}) and Untreated sample (29.4 μF·cm^{-2}). Since water has a much higher dielectric constant (≈80) than air (1) and paraffin (2.0–2.5), the increase in C_f directly demonstrates more water absorption of coating. Therefore, the HPS-P coating showed the best chemical inertness in 3.5 wt.% NaCl solution. The charge-transfer resistance (R_{ct}) represents the resistance to charge transfer during electrochemical processes and is directly related to the ease of corrosion reactions on metal surfaces. By systematically optimizing the laser parameters to form the HPS-3 architecture for maximum paraffin retention, the barrier performance was significantly enhanced. It can also be observed that the HPS-P coating exhibited a much higher R_{ct} (1.11 × 10^{11} Ω·cm^2), which was ca.8 and

ca.4 orders of magnitude higher than that of Untreated sample (5.09×10^3 Ω·cm^2) and HPS-S coating (4.78×10^7 Ω·cm^2), respectively. This indicates that HPS-P coating has the most effective corrosive ion barrier property.

Table 1. Fitted EIS results of different samples in 3.5 wt.% NaCl solution based on equivalent circuit models.

Parameter	Untreated	HPS-S	HPS-P
R_s (Ω·cm^2)	19.26	1.97×10^3	76.2
Y_f (S·cm^{-2}·sn)	3.19×10^{-5}	1.81×10^{-9}	5.58×10^{-11}
n_f	0.919	0.909	0.993
C_f (μF·cm^{-2})	29.4	1.21×10^{-3}	5.65×10^{-5}
R_f (Ω·cm^2)	1.20×10^4	9.94×10^6	/
Y_{dl} (S·cm^{-2}·s^n)	7.77×10^{-5}	7.26×10^{-8}	/
n_{dl}	0.418	0.828	/
C_{dl} (μF·cm^{-2})	21.1	9.4×10^{-2}	/
R_{ct} (Ω·cm^2)	5.09×10^3	4.78×10^7	1.11×10^{11}
Z_w (Ω^{-1}·s$^{0.5}$·cm^{-2})	/	8.22×10^{-15}	/
η_{EIS} (%)	/	99.99	>99.99

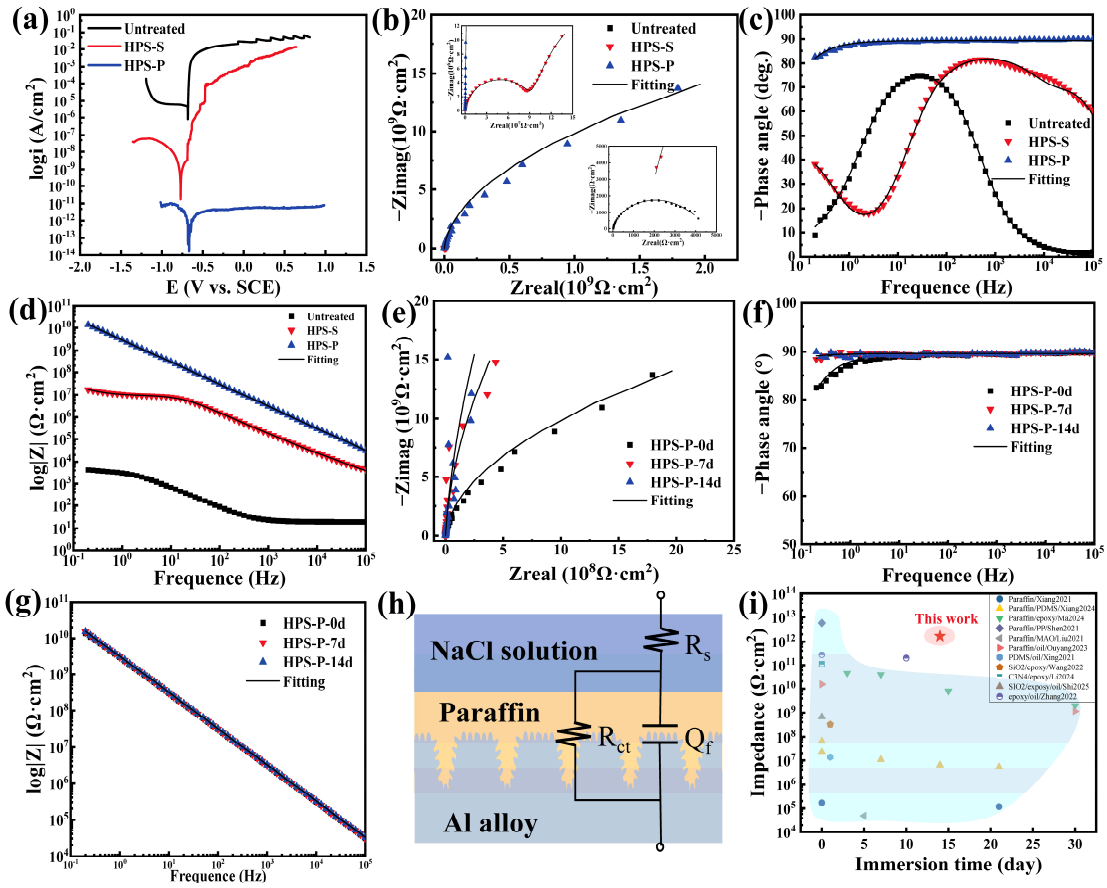


Figure 7. (**a**) Polarization curves of Untreated samples, HPS-S and HPS-P. EIS plots: (**b**) Nyquist plots; (**c**) Bode phase angle plots; (**d**) Bode impedance plots. The EIS plots of HPS-P after immersion in 3.5 wt.% NaCl solution for 14 days: (**e**) Nyquist plots; (**f**) Bode phase angle plots; (**g**) Bode impedance plots. (**h**) Equivalent circuit of HPS-P. (**i**) Comparison of the corrosion resistance of HPS-P coating with reported in self-healing coatings [5,20,22–26,44,45,49,53,54].

Generally, the inhibition efficiency (η_{EIS}) can be calculated from the EIS results by Equation (4) [55]. The η_{EIS} of HPS-P coating is >99.99% and effectively prevented the

corrosion reaction during the initial corrosion, indicates that the HPS-P coating has excellent barrier property for aluminum alloy substrates. In comparison, the η_{EIS} of HPS-S coating is 99.98935%, which also suggested that the HPS-P coating is more effective than HPS-S for preventing the invasion of corrosive medium to aluminum alloy substrates during immersion.

$$\eta_{EIS}(\%) = (1 - \frac{R_{ct}^0}{R_{ct}}) \times 100 \quad (4)$$

where R_{ct}^0 is the charge-transfer resistance of the Untreated aluminum alloy substrate, and R_{ct} is the charge-transfer resistance of the obtained HPS-S or HPS-P.

To investigate the long-term corrosion resistance of the HPS-P coating, EIS measurements were conducted after immersing in 3.5 wt.% NaCl solution for 0, 7, and 14 days (Figure 7e–g). Over the immersion period, The Bode phase angle approaching $-90°$ in the low-frequency region throughout the immersion period indicates the excellent barrier property and capacitive behavior of the coating. Detailed fitted EIS parameters are presented in Table 2. Compared with the initial immersion, the low-frequency impedance modulus $|Z|$ maintained a high value of 1.57×10^{10} $\Omega \cdot cm^2$ even after 14 days. Notably, across the 0, 7, and 14-day intervals, the charge transfer resistance (R_{ct}) exhibited an increasing trend, reaching 7.55×10^{11} $\Omega \cdot cm^2$ after 7 days and 1.67×10^{12} $\Omega \cdot cm^2$ after 14 days of immersion. This phenomenon is likely attributed to the localized formation of corrosion products (e.g., AlOOH) within minor structural defects, which effectively blocks ion migration channels. While the inherent chemical inertness of paraffin toward water is well known, conventional solid paraffin coatings suffer from rapid delamination in electrolytes due to poor interfacial adhesion and shrinkage stress. The structural novelty of the HPS-P coating lies in its ability to completely prevent this delamination, sustaining the paraffin's barrier properties over prolonged immersion. As shown in Figure 7i, although these reported systems involve diverse substrates and underlying mechanisms, this benchmark comparison demonstrates that the overall protective performance of the HPS-P coating is remarkably higher than that of previously reported self-healing coatings, including paraffin coatings [5,20,22–26,44,45,49,53,54].

Table 2. Fitted EIS results of HPS-P samples in 3.5 wt.% NaCl solution based on equivalent circuit models.

Parameter	HPS-P-0d	HPS-P-7d	HPS-P-14d
R_s ($\Omega \cdot cm^2$)	76.2	132.1	159.9
Y_f ($S \cdot cm^{-2} \cdot sn$)	5.58×10^{-11}	5.35×10^{-11}	5.16×10^{-11}
n_f	0.993	0.996	0.996
C_f ($\mu F \cdot cm^{-2}$)	5.65×10^{-5}	5.43×10^{-5}	5.27×10^{-5}
R_{ct} ($\Omega \cdot cm^2$)	1.11×10^{11}	7.55×10^{11}	1.67×10^{12}

Figure 8a,b show the SEM images of the HPS-P coating before and after immersion for 14 days. Before immersion, the coating surface was uniform and dense, and after immersion, small submicron particles appeared on the surface. This phenomenon is likely attributed to the deposition of corrosion products, such as AlOOH, formed by the local corrosion of the aluminum alloy substrate, which accumulates within coating defects. This deposition effectively blocks ion migration channels, thereby enhancing the coating's barrier property and consequently leading to the observed increase in R_{ct}. Figure 8c shows the FT-IR spectra before and after immersion for 14 days. Characteristic absorption bands at 2957 cm^{-1} (asymmetric methyl stretching), 2916 cm^{-1} (asymmetric methylene stretching), 2848 cm^{-1} (symmetric methylene stretching), 1472 cm^{-1} and 1462 cm^{-1} (methylene scissoring bending), and 1377 cm^{-1} (symmetric methyl bending) are consistent with the typical

features of long-chain alkanes (paraffin). Furthermore, the double peaks near 720 cm^{-1} suggest a highly ordered crystal structure, characteristic of solid-state paraffin. Crucially, the peak positions and intensities of the HPS-P coating remained virtually unchanged after 14 days of immersion, indicating its excellent chemical stability in NaCl solution. These results show that the HPS-P coating provides excellent and highly stable anti-corrosion performance, holding significant potential to extend the service life of aluminum alloys in corrosive environments.

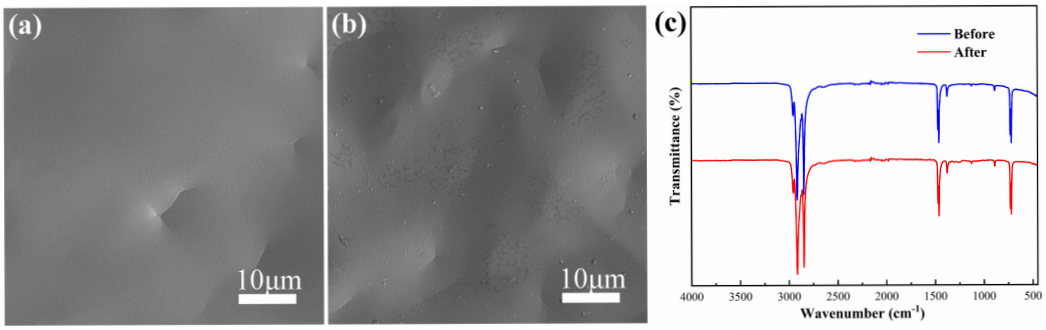


Figure 8. The SEM plots of the HPS-P coating in 3.5% NaCl solution for 14 days: (**a**) before, (**b**) after. (**c**) FT-IR spectra before and after immersion for 14 days.

4. Conclusions

In summary, this work develops a durable, thermally switchable anti-corrosion coating on aluminum alloy by integrating femtosecond laser-ablated hierarchical porous structures (HPS) with interfacial silanization and solid paraffin infusion. This strategy fundamentally addresses the persistent issue of lubricant depletion in conventional slippery surfaces. The structural stability of the HPS-P coating is sustained through a dual-locking mechanism: the laser-induced micro-grooves accommodate the volumetric shrinkage of paraffin to alleviate solidification stress, while the nano-clusters provide strong capillary adhesion. Concurrently, the OTES layer functions as a covalent bridge to enhance the chemical affinity between the inorganic substrate and the non-polar paraffin, ensuring a highly intact interface.

Exploiting the reversible phase-change properties of the solid lubricant, the surface exhibits thermally switchable wettability, transitioning from a protective pinning state at ambient temperature to a highly slippery state upon heating. The molten paraffin enables an active self-replenishing process that autonomously heals severe mechanical damage within approximately 100 s, driven by surface energy minimization. Consequently, the HPS-P coating effectively isolates the substrate from corrosive media, reducing the corrosion current density by six orders of magnitude compared to the bare aluminum alloy, and maintaining a high impedance modulus of ~10^{10} $\Omega \cdot cm^2$ even after 14 days of immersion in 3.5 wt.% NaCl solution. Furthermore, the coating maintains its hydrophobicity and structural integrity after repeated mechanical abrasion and environmental exposure (acid, alkali, and UV). This structural design strategy couples physical interlocking with dynamic chemistry, offering a highly viable approach for the long-term protection of lightweight aluminum infrastructure against chloride-induced degradation in marine engineering.

Supplementary Materials: The following supporting information can be downloaded at: https://www.mdpi.com/article/10.3390/coatings16030366/s1, Figure S1: Schematic diagram of femtosecond laser processing system. Figure S2. 3D images of HPS ablated by femtosecond laser. (a) HPS-1; (b) HPS-2; (c) HPS-3. Figure S3. EDS spectra. (a) HPS-1; (b) HPS-2; (c) HPS-3. Figure S4. XPS spectra. (a) Al 2 p of HPS-S; (b) C 1 s of HPS-S; (c) C 1 s of HPS-P. Figure S5. Sliding angle of HPS-S coating. Figure S6. Equivalent circuits for analyzing EIS plots. (a) Untreated; (b)HPS-S. Video S1: Video of

HPS-P coating during self-healing process. Video S2: Video of droplets on an inclined HPS-P surface before and after heating.

Author Contributions: Conceptualization, Z.Z.; methodology, Z.Z.; software, Z.Z.; validation, Z.Z., G.L. and Y.L.; formal analysis, Z.Z.; investigation, G.L.; resources, Z.Z.; data curation, Z.Z.; writing—original draft preparation, Z.Z.; writing—review and editing, Z.Z.; visualization, L.S.; supervision, L.S.; project administration, L.S.; funding acquisition, L.S. and G.L. All authors have read and agreed to the published version of the manuscript.

Funding: This work was supported by the National Natural Science Foundation of China (No. 52205354), the Hunan Provincial Natural Science Foundation of China (2023JJ40145), the China Postdoctoral Science Foundation (2022M711111), the State Key Laboratory of Advanced Design and Manufacturing Technology for Vehicle (32275002) and the Scientific Research Projects of Hunan Education Department (23B833).

Institutional Review Board Statement: Not applicable.

Informed Consent Statement: Not applicable.

Data Availability Statement: Data will be made available on request.

Conflicts of Interest: The authors declare no conflicts of interest.

References

1. Wong, T.S.; Kang, S.H.; Tang, S.K.; Smythe, E.J.; Hatton, B.D.; Grinthal, A.; Aizenberg, J. Bioinspired Self-Repairing Slippery Surfaces with Pressure-Stable Omniphobicity. *Nature* **2011**, *477*, 443–447. [CrossRef]
2. Yu, Z.; Zhang, H.; Yang, Y.; Wang, B.; Guo, Z. Slippery Liquid-Infused Porous Surfaces (SLIPS) for Anti-Icing. *Mater. Today* **2025**, *88*, 906–932. [CrossRef]
3. Ge, Y.; Song, Y.; Li, K.; Xuan, S.; Wang, L.; Liu, J.; Li, G.; Wang, X.; Yu, J.; Yang, Y.; et al. Highly Durable SLIPS with Temperature-Responsive Switching for Efficient Anti-/Deicing. *Chem. Eng. J.* **2025**, *507*, 160689. [CrossRef]
4. Zhao, Z.; Luo, G.; Cheng, M.; Song, L. Water-Repellent Coatings on Corrosion Resistance by Femtosecond Laser Processing. *Coatings* **2022**, *12*, 1736. [CrossRef]
5. Shi, Z.; Fang, C.; Li, J.; Bandaru, S.; Liu, M.; Zhao, L.; Zhang, X. Multi-Dimensional Design of Slippery Liquid-Infused Coatings Empowering Long-Term Corrosion Protection for Sintered Nd-Fe-B Magnets in Harsh Environments. *Small* **2025**, *21*, 2500629. [CrossRef] [PubMed]
6. Yong, J.; Chen, F.; Yang, Q.; Fang, Y.; Huo, J.; Zhang, J.; Hou, X. Nepenthes: Inspired Design of Self-Repairing Omniphobic Slippery Liquid Infused Porous Surface (SLIPS) by Femtosecond Laser Direct Writing. *Adv. Mater. Interfaces* **2017**, *4*, 1700552. [CrossRef]
7. Zhang, P.; Lin, L.; Zang, D.; Guo, X.; Liu, M. Designing Bioinspired Anti-Biofouling Surfaces Based on a Superwettability Strategy. *Small* **2017**, *13*, 1503334. [CrossRef]
8. Peppou-Chapman, S.; Hong, J.K.; Waterhouse, A.; Neto, C. Life and Death of Liquid-Infused Surfaces: A Review on the Choice, Analysis and Fate of the Infused Liquid Layer. *Chem Soc Rev* **2020**, *49*, 3688–3715. [CrossRef]
9. Tripathi, D.; Ray, P.; Singh, A.V.; Kishore, V.; Singh, S.L. Durability of Slippery Liquid-Infused Surfaces: Challenges and Advances. *Coatings* **2023**, *13*, 1095. [CrossRef]
10. Allachi, H.; Chaouket, F.; Draoui, K. Protection against Corrosion in Marine Environments of AA6060 Aluminium Alloy by Cerium Chlorides. *J. Alloys Compd.* **2010**, *491*, 223–229. [CrossRef]
11. Yimyai, T.; Crespy, D.; Rohwerder, M. Corrosion-Responsive Self-Healing Coatings. *Adv. Mater.* **2023**, *35*, 2300101. [CrossRef]
12. Adil, M.M.; Rabbi, M.S.; Tasnim, T. Development of Microcapsule-Based Self-Healing Composite: A Critical Review on Influencing Factors of Microencapsulation, Healing Efficiency, Thermal Stability and Application. *Alex. Eng. J.* **2025**, *122*, 1–17. [CrossRef]
13. Oehlenschlaeger, K.K.; Mueller, J.O.; Brandt, J.; Hilf, S.; Lederer, A.; Wilhelm, M.; Graf, R.; Coote, M.L.; Schmidt, F.G.; Barner-Kowollik, C. Adaptable Hetero Diels–Alder Networks for Fast Self-Healing under Mild Conditions. *Adv. Mater.* **2014**, *26*, 3561–3566. [CrossRef] [PubMed]
14. Tian, W.; Deng, J.; Higazy, S.A.; Selim, M.S.; Jin, H. Self-Healing Anti-Corrosion Coatings: Challenges and Opportunities from Laboratory Breakthroughs to Industrial Realization. *Coatings* **2025**, *15*, 620. [CrossRef]
15. Przybek, A.; Hebdowska-Krupa, M.; Łach, M. Paraffin Coated with Diatomite as a Phase Change Material (PCM) in Heat Storage Systems—A Review of Research, Properties, and Applications. *Materials* **2025**, *18*, 5166. [CrossRef]

16. Kang, C.; Sakaguchi, M.; Saito, A.; Inoue, H. Adhesion Strength of Paraffin Droplet Impacted and Solidified on Metal Substrate. *Results Phys.* **2022**, *34*, 105310. [CrossRef]
17. Ukrainczyk, N.; Kurajica, S.; Šipuši, J. Thermophysical Comparison of Five Commercial Paraffin Waxes as Latent Heat Storage Materials. *Chem. Biochem. Eng. Q* **2010**, *24*, 129–137.
18. Muhammad Ammar, S.; Duan, X.; Naterer, G.F. Effects of Surface Wettability and Density Change during Solidification of Paraffin Phase Change Materials. *Chem. Phys. Lett.* **2024**, *850*. [CrossRef]
19. Kang, C.; Sakaguchi, M.; Amano, A.; Kurokawa, Y.; Inoue, H. Quenching Stress and Fracture of Paraffin Droplet during Solidification and Adhesion on Metallic Substrate. *Surf. Coat. Technol.* **2019**, *374*, 868–877. [CrossRef]
20. Xiang, T.; Liu, J.; Liu, Q.; Wei, F.; Lv, Z.; Yang, Y.; Shi, L.P.; Li, C.; Chen, D.; Xu, G. Self-Healing Solid Slippery Surface with Porous Structure and Enhanced Corrosion Resistance. *Chem. Eng. J.* **2021**, *417*, 128083. [CrossRef]
21. Guo, Z.; Song, J.; Wang, G.; Zhao, G. Enhancing the Tribological and Corrosion Properties of 2A12 Aluminum Alloy via Micro-Arc Oxidation and Paraffin Sealing. *Colloids Surf. A Physicochem. Eng. Asp.* **2025**, *712*, 136476. [CrossRef]
22. Liu, Y.; Wen, S.; Liang, G.; Tian, G. Improvement in Corrosion Resistance of Micro-Arc Oxidized AZ91 Alloy Sealed with Cement-Mixed Paraffin Wax. *J. Mater. Sci. Technol.* **2021**, *15*, 6956–6973. [CrossRef]
23. Shen, T.; Liang, Z.-H.; Yang, H.-C.; Li, W. Anti-Corrosion Coating within a Polymer Network: Enabling Photothermal Repairing Underwater. *Chem. Eng. J.* **2021**, *412*, 128640. [CrossRef]
24. Ma, Q.-X.; Xu, L.; Fan, Y.; Wang, L.; Xu, J.-N.; Zhao, J.; Chen, X.-B. A Multifunctional Coating with Active Corrosion Protection through a Synergistic pH- and Thermal-Responsive Mechanism. *Small* **2024**, *20*, 2406912. [CrossRef]
25. Xiang, T.; Ren, H.; Zhang, Y.; Qiang, Y.; Yang, Y.; Li, C.; Wang, P.; Zhang, S. Rational Design of PDMS/Paraffin Infused Surface with Enhanced Corrosion Resistance and Interface Erosion Mechanism. *Mater. Des.* **2022**, *215*, 110450. [CrossRef]
26. Xiang, T.; Chen, X.; Guo, Z.; Wang, J.; Cui, L.; Qiang, Y.; Zhang, S. Robust Solid Slippery Surface for Anti-Corrosion: Experimental and Simulation. *Prog. Org. Coat.* **2024**, *188*, 108250. [CrossRef]
27. Ye, M.; Chen, W.; Wang, Y.; Zhao, R.; Xiao, W.; Li, J.; Meng, J.; Wang, S. Temperature-Driven Sustainable Anti-Scaling on Phase-Change Lubricant-Infused Surface. *Sci. China Mater.* **2024**, *67*, 2515–2522. [CrossRef]
28. Liang, S.; Zhao, X.; Zhang, W.; Huang, K.; Liu, W.; Li, J. Toward Sustainable and Durable Liquid-Infused Surfaces: A Review of Lubricant-Depletion Mitigation Strategies. *Chem. Commun.* **2025**, *61*, 19165–19182. [CrossRef]
29. Sahu, S.K.; Sonkar, M.; Rathore, S.K.; Naik, B.K. Sustainable Microencapsulated Phase Change Materials for Thermal Energy Storage Applications: A Comprehensive Review. *J. Therm. Anal. Calorim.* **2026**. [CrossRef]
30. Vorobyev, A.Y.; Guo, C. Direct Femtosecond Laser Surface Nano/Microstructuring and Its Applications. *Laser Photonics Rev.* **2013**, *7*, 385–407. [CrossRef]
31. Gao, L.; Zhang, Q.; Gu, M. Femtosecond Laser Micro/Nano Processing: From Fundamental to Applications. *Int. J. Extrem. Manuf.* **2024**, *7*, 022010. [CrossRef]
32. Love, J.C.; Estroff, L.A.; Kriebel, J.K.; Nuzzo, R.G.; Whitesides, G.M. Self-Assembled Monolayers of Thiolates on Metals as a Form of Nanotechnology. *Chem. Rev.* **2005**, *105*, 1103–1170. [CrossRef]
33. Nicosia, C.; Huskens, J. Reactive self-assembled monolayers: From surface functionalization to gradient formation. *Mater. Horiz.* **2014**, *1*, 32–45. [CrossRef]
34. Pujari, S.P.; Scheres, L.; Marcelis, A.T.M.; Zuilhof, H. Covalent Surface Modification of Oxide Surfaces. *Angew. Chem. Int. Ed.* **2014**, *53*, 6322–6356. [CrossRef] [PubMed]
35. Zhu, D.; Van Ooij, W.J. Corrosion Protection of AA 2024-T3 by Bis-[3-(Triethoxysilyl)Propyl] Tetrasulfide in Neutral Sodium Chloride Solution. Part 1: Corrosion of AA 2024-T3. *Corros. Sci.* **2003**, *45*, 2163–2175. [CrossRef]
36. Hadhri, M.; Colleoni, C.; D'Agostino, A.; Erhaim, M.; Rosa, R.P.; Rosace, G.; Trovato, V. Eco-Friendly Octylsilane-Modified Amino-Functional Silicone Coatings for a Durable Hybrid Organic–Inorganic Water-Repellent Textile Finish. *Polymers* **2025**, *17*, 1578. [CrossRef] [PubMed]
37. Gao, X.; Guo, Z. Mechanical Stability, Corrosion Resistance of Superhydrophobic Steel and Repairable Durability of Its Slippery Surface. *J. Colloid Interface Sci.* **2017**, *512*, 239–248. [CrossRef]
38. Jiang, D.; Xia, X.; Hou, J.; Cai, G.; Zhang, X.; Dong, Z. A Novel Coating System with Self-Reparable Slippery Surface and Active Corrosion Inhibition for Reliable Protection of Mg Alloy. *Chem. Eng. J.* **2019**, *373*, 285–297. [CrossRef]
39. Ni, X.; Li, C.; Lei, Y.; Shao, Y.; Zhu, Y.; You, B. Design of a Smart Self-Healing Coating with Multiple-Responsive Superhydrophobicity and Its Application in Antibiofouling and Antibacterial Abilities. *ACS Appl. Mater. Interfaces* **2021**, *13*, 57864–57879. [CrossRef]
40. Jiao, Z.; Zhou, Y.; Dai, X.; Wu, J.; Chen, Y.; Wu, M.; Yao, W.; Yuan, Y.; Xie, Z.; Ma, Y.; et al. A Bimodified MgAlCe-LDHs@GO Self-Healing Anti-Corrosion Coating Based on the Micro Arc Oxidation Coating of AZ31 Magnesium Alloy. *Corros. Sci.* **2025**, *248*, 112805. [CrossRef]

41. Zhang, S.; Shen, Y.; Lu, J.; Chen, Z.; Li, L.; Guo, F.; Shi, W. Tannic Acid-Modified g-C3N4 Nanosheets/Polydimethylsiloxane as a Photothermal-Responsive Self-Healing Composite Coating for Smart Corrosion Protection. *Chem. Eng. J.* **2024**, *483*, 149232. [CrossRef]
42. Hao, Z.; Chen, C.; Shen, T.; Lu, J.; Yang, H.-C.; Li, W. Slippery Liquid-Infused Porous Surface via Thermally Induced Phase Separation for Enhanced Corrosion Protection. *J. Polym. Sci.* **2020**, *58*, 3031–3041. [CrossRef]
43. Rao, Q.; Li, A.; Zhang, J.; Jiang, J.; Zhang, Q.; Zhan, X.; Chen, F. Multi-Functional Fluorinated Ionic Liquid Infused Slippery Surfaces with Dual-Responsive Wettability Switching and Self-Repairing. *J. Mater. Chem. A* **2019**, *7*, 2172–2183. [CrossRef]
44. Li, X.; Liu, H.; Meng, S.; Wang, F.; Mei, T.; Cai, X.; Ran, Y. Smart Epoxy Coating: G-C3N4 Nanosheets Loaded MOFs for Enhanced Anti-Corrosion and UV Resistance. *Chem. Eng. J.* **2024**, *488*, 150731. [CrossRef]
45. Xing, K.; Li, Z.; Wang, Z.; Qian, S.; Feng, J.; Gu, C.; Tu, J. Slippery Coatings with Mechanical Robustness and Self-Replenishing Properties as Potential Application on Magnesium Alloys. *Chem. Eng. J.* **2021**, *418*, 129079. [CrossRef]
46. Qiu, S.; Sun, T.-Y.; Su, Y.; Huang, L.-F.; Zhao, H.; Xue, Q.; Wang, L. Construction of Hierarchical Nanocarrier via a "MOFs plus Graphene" Strategy for Sustained Release and Rust-Induced Self-Healing. *Chem. Eng. J.* **2021**, *426*, 131879. [CrossRef]
47. Zhuo, Y.; Håkonsen, V.; He, Z.; Xiao, S.; He, J.; Zhang, Z. Enhancing the Mechanical Durability of Icephobic Surfaces by Introducing Autonomous Self-Healing Function. *ACS Appl. Mater. Interfaces* **2018**, *10*, 11972–11978. [CrossRef]
48. Zhang, H.; Liang, Y.; Wang, P.; Zhang, D. Design of Slippery Organogel Layer with Room-Temperature Self-Healing Property for Marine Anti-Fouling Application. *Prog. Org. Coat.* **2019**, *132*, 132–138. [CrossRef]
49. Wang, J.; Ma, L.; Guo, X.; Wu, S.; Liu, T.; Yang, J.; Ren, C.; Li, S.; Zhang, D. Two Birds with One Stone: Nanocontainers with Synergetic Inhibition and Corrosion Sensing Abilities towards Intelligent Self-Healing and Self-Reporting Coating. *Chem. Eng. J.* **2022**, *433*, 134515. [CrossRef]
50. Cassie, A.B.D.; Baxter, S. Wettability of Porous Surfaces. *Trans. Faraday Soc.* **1944**, *40*, 546–551. [CrossRef]
51. *ATSM D3359*; Standard Test Methods for Rating Adhesion by Tape Test. American Society for Testing and Materials: West Conshohocken, PA, USA, 2023.
52. Li, D.-W.; Wang, H.-Y.; Liu, Y.; Wei, D.-S.; Zhao, Z.-X. Large-Scale Fabrication of Durable and Robust Super-Hydrophobic Spray Coatings with Excellent Repairable and Anti-Corrosion Performance. *Chem. Eng. J.* **2019**, *367*, 169–179. [CrossRef]
53. Ouyang, Y.; Kang, H.; Guo, E.; Qiu, R.; Su, K.; Chen, Z.; Wang, T. Thermo-Driven Oleogel-Based Self-Healing Slippery Surface Behaving Superior Corrosion Inhibition to Mg-Li Alloy. *J. Magnes. Alloy* **2023**, *11*, 4710–4723. [CrossRef]
54. Zhang, M.; Chen, P.; Li, J.; Wang, G. Water-Repellent and Corrosion Resistance Properties of Epoxy-Resin-Based Slippery Liquid-Infused Porous Surface. *Prog. Org. Coat.* **2022**, *172*, 107152. [CrossRef]
55. Zhang, X.-F.; Chen, Y.-Q.; Hu, J.-M. Robust Superhydrophobic SiO2/Polydimethylsiloxane Films Coated on Mild Steel for Corrosion Protection. *Corros. Sci.* **2020**, *166*, 108452. [CrossRef]

Disclaimer/Publisher's Note: The statements, opinions and data contained in all publications are solely those of the individual author(s) and contributor(s) and not of MDPI and/or the editor(s). MDPI and/or the editor(s) disclaim responsibility for any injury to people or property resulting from any ideas, methods, instructions or products referred to in the content.